GDCh

Research Article

Angewandte
Chemie
International Edition
www.angewandte.org

VIP Metal–Organic Frameworks | *Very Important Paper*

Engineering a Meltable MOF to Tune Liquid Transition and Promote Coenzyme Regeneration

Wengang Huang, Wen-Long Xue, Peng Chen, Zhiliang Wang, Rijia Lin, Shuke Zhao, Shuwen Yu, Yuelei Chen, Xiangyi Zha, Dominique Appadoo, Tian Tian, Vicki Chen, Sebastian Henke, Anthony K. Cheetham, Lianzhou Wang, and Jingwei Hou*

Abstract: Modulating the liquid phase of metal–organic frameworks (MOFs) presents new opportunities for functionalizing glassy MOFs, expanding the fundamental science and practical application for this emerging family of materials. Herein, we report the fabrication of a bimetallic glassy MOF via a liquid–liquid transition process. This is achieved by introducing a robust Schiff base–cobalt functional group into Zn-ZIF-62, which attracts negatively charged imidazolate ligands, facilitating low-temperature melting. This ultimately leads to the formation of a bimetallic glassy MOF (Co/Zn-a$_g$ZIF-62-ipy) upon melt-quenching. The material features an exceptionally high glass-forming capability, uniformly distributed bimetallic ions, and a markedly enhanced visible light photogeneration efficiency of enzymatically active nicotinamide adenine dinucleotide (NADH) when compared with Co-doped ZIF-62 glass. These findings offer novel insights into modulating the liquid phase of an MOF to develop functional glassy MOF photocatalysts for coenzyme NADH regeneration and other advanced applications.

Introduction

The natural photosystem I (PS I) harnesses solar energy to drive the reduction of coenzyme nicotinamide adenine dinucleotide (NAD(P)$^+$) into its reduced form NAD(P)H (H for hydrogen), representing a critical step in the conversion of light energy into chemical forms.[1] The NAD(P)H can then be applied in several subsequent biological reactions, such as oxidative phosphorylation in the electron transport chain, fermentation processes, fatty acid biosynthesis, and various enzymatic reactions requiring reducing power. In recent decades, various approaches have been explored to mimic PS I and regenerate NADH, including biological, electrochem-

ical, and photocatalytic pathways.[2–4] Photocatalytic NADH regeneration, distinguished by its ecological, economic, and sustainable features, has recently garnered significant attention.[5] Currently, photocatalytic NADH regeneration typically necessitates the presence of semiconductor photocatalysts and, in particular, the addition of a homogeneous mediator, e.g. [Cp*Rh(bpy)H$_2$O]$^{2+}$, which acts as a redox mediator for transferring electrons and protons.[6] However, simultaneously involving a semiconductor photocatalyst and a metal-complex mediator in the photocatalytic regeneration of NADH often escalates the cost and complexity of the reaction.[7] To date, numerous endeavors have been undertaken to integrate photocatalysts with Rh-complex mediators

[*] W. Huang, Z. Wang, R. Lin, S. Zhao, S. Yu, Y. Chen, X. Zha,
Prof. L. Wang, Associate Prof. J. Hou
School of Chemical Engineering, The University of Queensland,
Saint Lucia, QLD 4072, Australia
E-mail: jingwei.hou@uq.edu.au

W.-L. Xue, Prof. S. Henke
Anorganische Chemie, Fakultät für Chemie und Chemische Biologie,
Technische Universität Dortmund, Otto-Hahn Straße 6 44227,
Dortmund, Germany

P. Chen
Australian Institute for Bioengineering and Nanotechnology, The
University of Queensland, Saint Lucia, QLD 4072, Australia

D. Appadoo
Australian Synchrotron, 800 Blackburn Rd, Clayton, VIC 3168,
Australia

T. Tian
Department of Applied Biology and Chemical Technology, The Hong
Kong Polytechnic University, Hung Hom, Hong Kong SAR, P.R.
China

Prof. V. Chen
University of Technology Sydney, 15 Broadway, Ultimo, NSW 2007,
Australia

Prof. A. K. Cheetham
Materials Research Laboratory, University of California, Santa
Barbara, CA 93106, USA

Associate Prof. J. Hou
ARC Centre of Excellence for Green Electrochemical Transformation
of Carbon Dioxide, Brisbane 4072, Australia

aiming for a higher NADH yield, e.g., the covalent binding of polymeric carbon nitride with grafted mediators,[8] the conjunction of covalent organic frameworks and mediators,[7] and the immobilization of mediators within porous crystalline structures.[9] Despite these advances, current endeavors still mostly focus on immobilizing costly noble metal-based Rh complexes, and the reported activity of the photocatalysts remains far from satisfactory. Consequently, the construction of an integrated structure that directly channels the photogenerated carriers to a non-noble metal mediator offers a highly desirable strategy for photocatalytic NADH regeneration, particularly if it is driven by visible light.[10]

The regeneration of NADH facilitated by the earth-abundant 3d metal site is of significant interest but remains relatively uncommon in the literature. Cobalt-based compounds have been recognized for their efficacy in proton reduction and hydrogen production.[11,12] Building on this foundation, systems incorporating a cobalt catalyst have demonstrated considerable potential for the photogeneration of enzymatically active NADH.[13] The incorporation of cobalt atoms into metal–organic frameworks (MOFs) can be highly desirable for acting as redox mediators, given that the MOF matrix exhibits numerous chemical and electrical properties that resemble those of metalloenzymes and metal-complex catalysts.[14–16] However, cobalt atoms, serving as the primary metal centers in MOF structure may exhibit insufficient stability; for instance, ZIF-67, a Co-based MOF consisting of Co^{2+} ions and imidazolate ligands, features weak Co-imidazolate coordination bonds and has limited stability under catalytic conditions.[17,18] Additionally, incorporating cobalt ions through adsorption may result in the formation of undesirable cobalt-based oxides or phase segregation, further compromising catalytic performance or structure compatibility. By contrast, Schiff base–cobalt complexes provide well-defined coordination environments that stabilize cobalt in catalytically active oxidation states, improving its electron transfer kinetics and redox cycling efficiency.[19] The strong chelating ability of Schiff bases helps regulate the electronic properties of the cobalt center, which can fine-tune its photocatalytic activity for NADH regeneration.[20,21] MOFs are distinguished by the spatial isolation of metal centers through ligands and a highly tunable surface area.[22] They demonstrate flexibility in the modification of metal nodes and organic ligands. In addition, it can also serve as a scaffold to immobilize secondary metal centers, e.g., 3d metals, via de novo linker functionalization or postsynthetic modification methods.[23] Therefore, the integration of Schiff base–cobalt units within Zn-based MOF architectures via postsynthetic modification enables access to the different properties of the constituent elements and, potentially, may give rise to new and intriguing properties as a result of the synergetic effect.[24,25]

The discovery and recent development of meltable MOFs and MOF glasses have further broadened the scope of MOF functionalization.[26–28] This is due to the inherent nature of melting and vitrification processes, which involve the transient cleavage and reformation of chemical bonds during melting, as well as the liquid–liquid transition process. These provide an ideal platform for bulk-phase MOF functionalization through the incorporation of secondary metal centers or additional ligands. High-density amorphous liquid MOFs and their low-density counterparts exhibit very similar short-range order to the parental MOFs while retaining a microporous structure capable of efficiently harnessing light through multiple scattering.[29–31] This liquid–liquid transition process can offer a new avenue for biomimetic photocatalyst development, enabling metalation and recoordination of ligand bearing metal ions to effectively replicate the secondary coordination environment of metalloenzymes.[32] Thus, we are inspired to engineer meltable MOFs and explore the benefits of their non-noble secondary metal center for artificial photocatalysis.

Herein, we describe a method to precisely tune the coordination structure of a bimetallic MOF glass to emulate the structure and function of metalloenzymes. This is achieved by incorporating Schiff base–Co units into a meltable Zn-MOF through linker functionalization. Upon heating, a liquid–liquid phase transformation enables the uniform and consistent metalation of a secondary metal within the framework, allowing precise control over the coordination environment of both metal ions. The resulting MOF glass stabilizes this tailored structure, replicating the synergistic function of natural bimetallic enzymes—one metal enhances catalytic performance, whereas the other provides structural stability.[33] The liquid modification strategy imparts meltable MOFs with unique properties, granting them exceptionally high glass forming capability and enhanced photocatalytic activity for NADH regeneration.

Results and Discussion

Materials Structural Characterization

Crystalline Zn-ZIF-62-NH$_2$ with an overall composition of [Zn(imidazole)$_{1.9}$(5-aminobenzimdazole)$_{0.1}$] was fabricated by a solvothermal method. It is subsequently referred to as ZIF-62-NH$_2$ for simplicity; ^{1}H NMR analysis confirmed the ligand ratio, as shown in Figure S1. Then, ipy (where ipy denotes the iminopyridine functional group) and cobalt ions were introduced by postsynthetic modification (see Supporting Information).[32,34] In order to achieve this, the aldehyde groups of 2-pyridinecarboxaldehyde were reacted with the amino groups of ZIF-62-NH$_2$ through the Schiff-base condensation reaction, thereby incorporating the iminopyridine moieties into the framework (ZIF-62-ipy). Then, the iminopyridine moiety could be employed to anchor the secondary metallic atoms, e.g., Co atoms in this case, to form Schiff base–cobalt units via mixing with Co(OAc)$_2$·4H$_2$O in methanol. Scheme 1 depicts the detailed changes in the chemical structure during the modification process and the subsequent melt-quenching, whereas Figure S2 shows a photo of the modified samples. The resultant sample was denoted as Co/Zn-ZIF-62-ipy. The successful incorporation of the iminopyridine functional group was confirmed by employing electrospray ionization mass spectrometry (ESIMS) on the fully digested Co/Zn-ZIF-62-ipy. The result revealed an ion peak at m/z 223.2 ([M+H]$^+$) corresponding to the functionalized linker fragments containing the iminopyridine
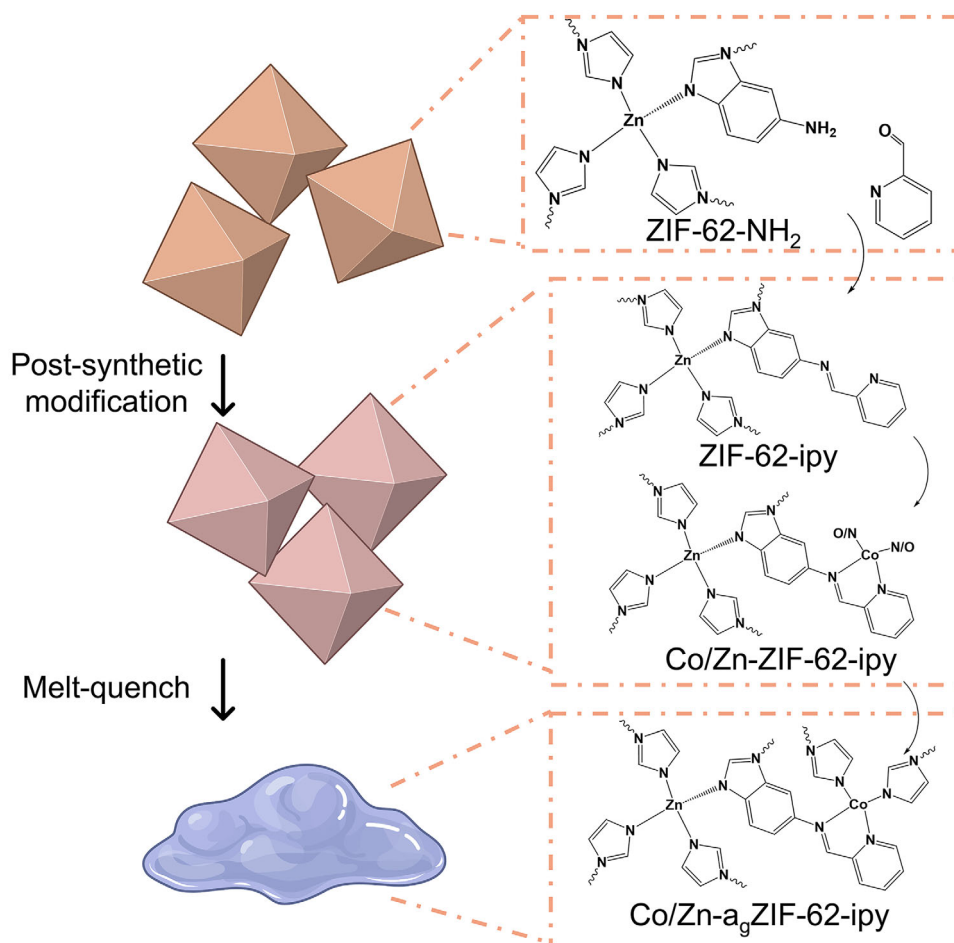
Scheme 1. Postsynthetic functionalization pathway of ZIF-62-NH$_2$.

unit (Figure 1a). Liquid chromatography–mass spectrometry (LCMS) further substantiates the presence of modified linkers incorporating the iminopyridine unit (Figure S3). ^{1}H NMR analysis of digested samples further confirmed that more than half of the amino groups are functionalized by iminopyridine (Figure S4), indicating that the linker functionalization extends beyond the surface layer.[27,32,35] Furthermore, CHN elemental analysis (Table S1) verifies a reduced N/C ratio for ZIF-62-ipy and Co/Zn-ZIF-62-ipy (about 0.680) compared to pristine ZIF-62-NH$_2$ (approximately 0.700), indicating the successful incorporation of 2-pyridinecarboxaldehyde. Bimetallic glass can then be prepared by subjecting Co/Zn-ZIF-62-ipy to melt-quenching treatment.

The introduction of iminopyridine moiety did not lead to significant changes in the crystal structure according to the powder X-ray diffraction (PXRD) patterns (Figure 1b). However, the postsynthetic modification process, coupled with continuous magnetic stirring, may induce fragmentation of MOF particles and generate surface defects, thereby promoting the exposure of specific crystal facets and contributing to particle size reduction. This is consistent with the scanning electron microscopy observations (Figure 1c–e) and high-resolution transmission electron microscopy (HRTEM) image (Figure 1f), which show a notable decrease in particle

size following the modification procedure. Both amino- and imine-functionalized MOFs generally exhibit preferable CO$_2$ adsorption behaviors due to their increased polarity and the ability of nitrogen-containing groups to engage in dipole–quadrupole interactions with CO$_2$ molecules.[36–39] Accordingly, as shown in Figure 1g, the CO$_2$ isotherm of Co/Zn-ZIF-62-ipy that features imine functionalities introduced via Schiff base displays only a slight reduction in uptake compared to ZIF-62-NH$_2$, despite the bulkier nature of the ipy ligand. This is likely due to the limited extent of functionalization, which only partially occupies pore volume. This interpretation is further supported by the pore size distribution data (Figure 1h), which shows no significant change, indicating retention of the overall framework and porosity. Additionally, the inset of Figure 1g indicates that the initial slope of Co/Zn-ZIF-62-ipy isotherm is less steep than that of the pristine crystal, which aligns with the ^{1}H NMR analysis (Figure S4), showing that linker functionalization is not restricted to the limited number of amino groups present on the surface but also occurs within the internal micropores. The Pawley refinement of ZIF-62-NH$_2$, ZIF-62-ipy, and Co/Zn-ZIF-62-ipy further substantiate the unit cell change of ZIF-62-ipy and Co/Zn-ZIF-62-ipy due to the introduction of iminopyridine and Schiff base–cobalt
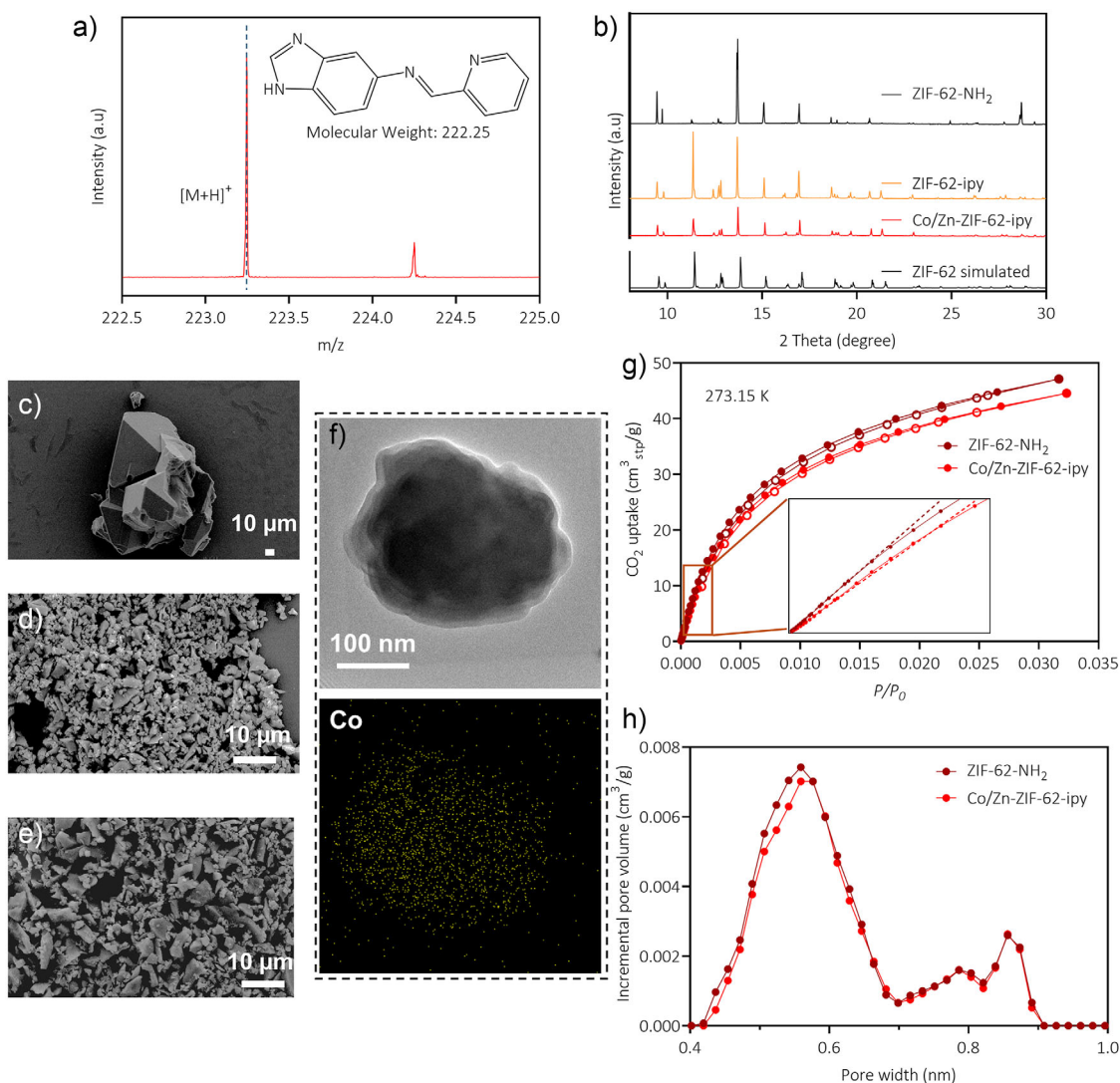
Figure 1. a) ESI-mass spectrum of modified linkers fragment from Co/Zn-ZIF-62-ipy. b) PXRD patterns of ZIF-62-NH$_2$ and its derivative ZIF-62-ipy and Co/Zn-ZIF-ipy and Co/Zn-ZIF-62-ipy. c) SEM image of ZIF-62-NH$_2$, d) SEM image of ZIF-62-ipy, and e) SEM image of Co/Zn-ZIF-ipy. F) HRTEM image of Co/Zn-ZIF-62-ipy particle and Co element mapping. g) CO$_2$ adsorption–desorption isotherms of ZIF-62-NH$_2$ and Co/Zn-ZIF-62-ipy at 273.15 K. h) Pore size distribution of ZIF-62-NH$_2$ and Co/Zn-ZIF-62-ipy.

complex. As shown in Figure S5, the ZIF-62-ipy, Co/Zn-ZIF-62-ipy, and ZIF-62-NH$_2$ are of the same space group *Pbca*, whereas the modified ZIF-62-ipy and Co/Zn-ZIF-62-ipy exhibit an expanded unit cell relative to unmodified ZIF-62-NH$_2$. Furthermore, HRTEM energy-dispersive X-ray (EDX) mapping of Co/Zn-ZIF-62-ipy (Figures 1F and S6) demonstrates that the distribution of cobalt is correlated with the crystal thickness, further substantiating the formation of Schiff base–cobalt moieties beyond the surface.

The Fourier transform infrared (FTIR) spectroscopy was implemented to further confirm the variation of functional groups (Figures 2a and S7). Figure S7 confirms that ZIF-62-NH$_2$ exhibits two amino stretching modes at 3363 and 3105 cm^{-1} for the asymmetric and symmetric stretching vibrations, respectively. The intensity of these two peaks drops after modification, substantiating the functionalization of the amino group.[40] The FTIR spectra (Figure 2a) of

modified samples, ZIF-62-ipy and Co/Zn-ZIF-62-ipy, were very similar, with the peak at ca. 740 cm^{-1} being assigned to the vibrations of C—H from pyridine rings, whereas the in-plane ring deformation band of pyridine was found at 705 cm^{-1}. In comparison, these two features were not observed from the pristine ZIF-62-NH$_2$. The peak at around 1580–1590 cm^{-1} is attributable to the stretching vibration of the azomethine group ν(C=N) as the modified samples demonstrated enhanced absorption in this region due to the incorporation of C=N from Schiff base condensation.[41,42] The Schiff base–cobalt complex from Co/Zn-ZIF-62-ipy also displayed a peak at 465 cm^{-1} due to Co—N bonds, confirming the coordination of the Co to the Schiff base via azomethine and pyridyl nitrogen atoms.[40]

ZIF-62-NH$_2$ and Co/Zn-ZIF-62-ipy were subsequently thermally treated to 400 °C and then quenched back to room temperature under an argon atmosphere for the
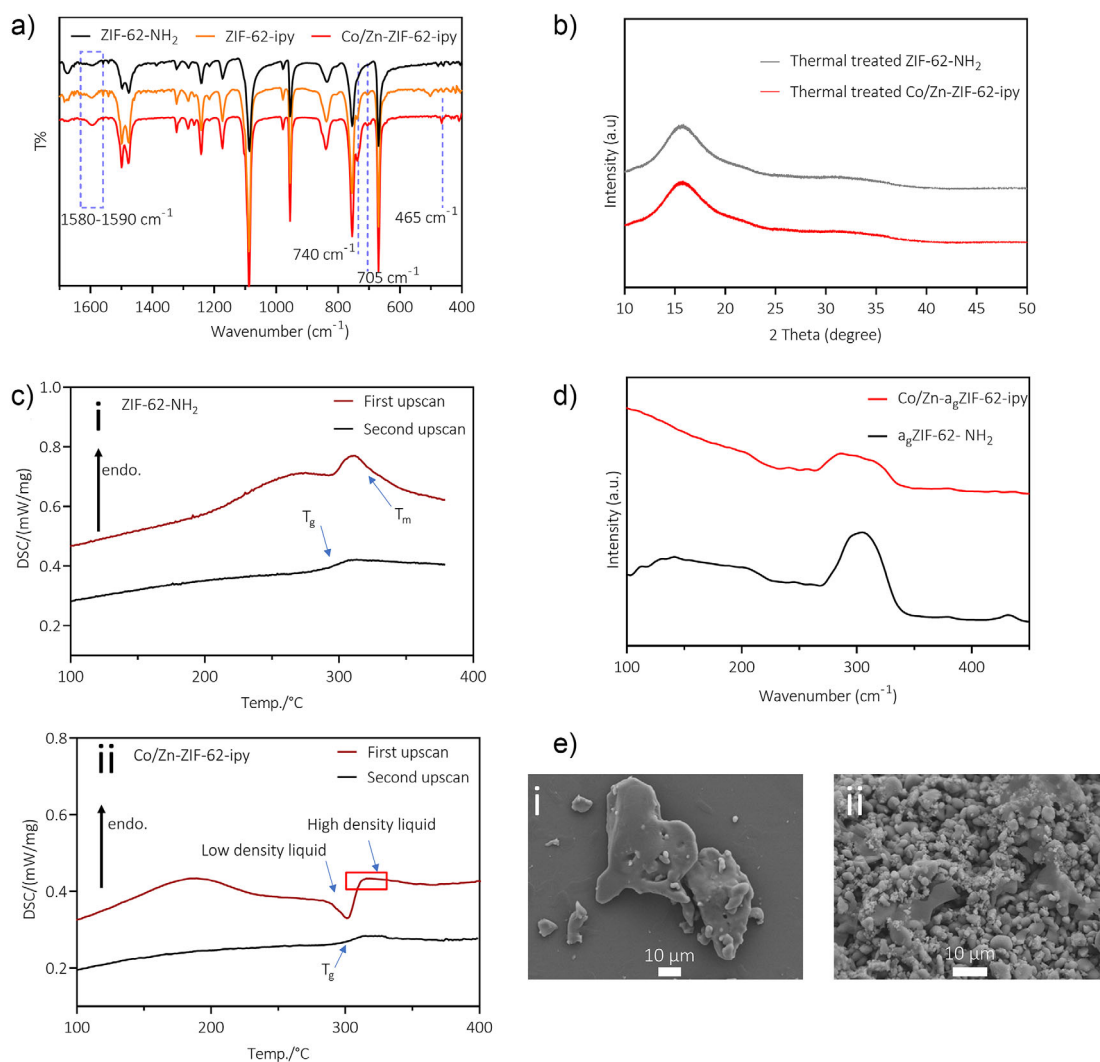
Figure 2. a) FTIR patterns of ZIF-62-NH$_2$ and its derivative ZIF-62-ipy and Co/Zn-ZIF-ipy. b) PXRD patterns of a_gZIF-62-NH$_2$ and Co/Zn-a_gZIF-62-ipy. c) DSC curves of (i) ZIF-62-NH$_2$ and (ii) Co/Zn-ZIF-ipy, the first upscan recorded the LLT and the second upscan exhibited T_g. d) THz/Far-IR spectrums for a_gZIF-62-NH$_2$ and Co/Zn-a_gZIF-62-ipy. e) SEM image of (i) a_gZIF-62-NH$_2$ and (ii) Co/Zn-a_gZIF-62-ipy.

melting and subsequent glass formation. PXRD patterns confirm that the materials are amorphous after the thermal treatment, with no evidence of metal oxide (i.e., CoO or Co$_2$O$_3$) or metal nanoparticle formation (Figure 2b). The amorphous structures of the thermal treated samples were further observed using high-resolution transmission electron microscopy (HRTEM). Additionally, energy-dispersive X-ray spectroscopy (EDS) mapping analysis confirmed the uniform distribution of Co atoms within the treated sample, as shown in Figure S8.

To probe the influence of the modified linkers upon heating, differential scanning calorimetry (DSC) thermal analyses of the ZIF-62-NH$_2$ and Co/Zn-ZIF-62-ipy were performed under a continuous flowing Ar atmosphere. The DSC trace for ZIF-62-NH$_2$ exhibited a simple endothermic peak attributed to crystal melting at ca. 340 °C (offset, Figure 2c(i)), a melting temperature in good agreement with ZIF-62 containing secondary 5-aminobenzimidazole linkers reported in the literature.[27] In comparison, the Co atoms

anchored sample Co/Zn-ZIF-62-ipy displayed consecutively exothermic and endothermic features within the temperature range of 275–350 °C in the first upscan and also displayed a glass transition in the second scan (Figure 2c(ii)).

The thermal behavior of the modified sample here is distinctive, yet it is comparable to the reported behavior of ZIF-4.[30] The initial exothermic signal can be attributed to the collapse of the crystalline frameworks into a low-density liquid (LDL) or amorphous phase, whereas the endothermic peak that follows indicates the liquid–liquid transition (LLT), which is the transition from the LDL to the high-density liquid (HDL).[31] The low-density liquid transition behavior below 300 °C is also validated by in situ XRD pattern, as shown in Figure S9. Upon heating to temperatures exceeding 250 °C, all the XRD peaks of Co/Zn-ZIF-62-ipy undergo a positive shift to a higher angle, indicating a transition to a more compact state. Upon heating to 350 °C, the modified material completed the melting process. The thermogravimetric analysis (Figure S10) indicates that, apart from desolvation, neither

ZIF-62-NH$_2$ nor Co/Zn-ZIF-62-ipy exhibited any significant weight loss during the melting process.

To further investigate this unique thermal behavior, DSC measurements were done on samples with different amounts of cobalt-anchored iminopyridine linkers (Figure S11A shows the DSC result, and Table S2 shows the different Co/Zn ratio). With more cobalt-anchored iminopyridine linkers (Co/Zn ratio ca. 0.035), the materials gradually exhibit a reduction in initial exothermic enthalpy, as shown in Figure S11B. The enthalpy release changed from −4.15 J g^{-1} to −2.92 J g^{-1}, primarily due to the enhanced steric effects contributed by modified linkers. These steric effects may hinder framework mobility and flexibility, thereby restricting the crystal's ability to reorganize into a low-density liquid or amorphous phase. In contrast, with more functionalized linkers, the endothermic peak intensified. Based on DSC calculation, with more cobalt-anchored iminopyridine linkers, higher thermal energy is required to achieve the melting process. This suggests the functionalized linkers have been effectively incorporated within the MOF matrix, leading to higher bonding energy between metal nodes and ligands, thereby more thermal energy is required for the phase transition. Consequently, as shown in Figure 2c(ii), the onset temperature of the exothermic framework could be regarded as the onset temperature for Co/Zn-ZIF-62-ipy melting. The melting of the Co/Zn-ZIF-62-ipy is completed at the offset temperature of the endothermic LDL-to-HDL transition. The offset melting point is ca. 350 °C, slightly higher than T_g (mid, ca. 300 °C) obtained from the second upscan, indicating a very strong resistance to recrystallisation and high glass forming capability. The amorphous materials are named a$_g$ZIF-62 and Co/Zn-a$_g$ZIF-62-ipy, respectively, where a$_g$ represents amorphization through melting.

To probe the coordinative environment variations upon heating and provide evidence for the interaction between secondary metal nodes and imidazolate ligands, synchrotron THz/Far-IR spectroscopy characterization was performed with a$_g$ZIF-62-NH$_2$ and Co/Zn-a$_g$ZIF-62-ipy (Figure 2d). The glassy Co/Zn-a$_g$ZIF-62-ipy exhibits a broader peak at ca. 290 cm^{-1} in comparison to the unmodified a$_g$ZIF-62-NH$_2$, which confirms anchored Co atoms can alter the oscillation or stretching movements between Zn and imidazole.[28,43,44] SEM also distinguishes glass features of a$_g$ZIF-62-NH$_2$ and Co/Zn-a$_g$ZIF-62-ipy, as shown in Figures 2e(i) and (ii) and S12; instead of merging together, the Co/Zn-a$_g$ZIF-62-ipy samples form separate glassy beads, which can be mainly attributed to the lower surface energy caused by functionalized ligands.

Probing Co Coordination Environment Before and After the Vitrification Process

To elucidate the electronic environment of the low concentration of cobalt in Co/Zn-ZIF-62-ipy and Co/Zn-a$_g$ZIF-62-ipy, multiple X-ray photoelectron spectroscopy (XPS) scans were conducted on Co 2p to ensure detection and analysis. Despite the relatively low signal due to the low cobalt loading, the spectra provided features for XPS fitting, as shown in

Figure S13. The Co 2p$_{3/2}$ and 2p$_{2/1}$ peaks, along with the corresponding satellite features, are indicative of Co (II) state. To further reveal the local structure of Co atoms prior to and after the vitrification process and provide evidence for the formation of secondary metal centers, the electronic structures and coordination environments of Co sites in Co/Zn-ZIF-62-ipy and Co/Zn-a$_g$ZIF-62-ipy were investigated by highly sensitive synchrotron X-ray absorption spectroscopy (XAS) in fluorescence mode. In comparison to Co foil and Co(OAc)$_2$·4H$_2$O, an intense pre-edge peak ca. 7710 eV can be observed in the near-edge region of both Co/Zn-ZIF-62-ipy and Co/Zn-a$_g$ZIF-62-ipy. This pre-edge peak is indicative of the 1s→3d electronic transition, which is forbidden in centrosymmetric compounds having an octahedral environment surrounding Co atoms. Consequently, the existence of the pre-edge feature demonstrates that the local environment of Co atoms lacks a center of symmetry and corroborates the anticipated tetrahedral coordination geometry (Figure 3a).[45] The formation of a slightly higher pre-edge peak in glassy Co/Zn-a$_g$ZIF-62-ipy distinguishes the enhanced tetrahedral geometry of the Co coordination environment from that of the Co/Zn-ZIF-62-ipy crystal. Moreover, the anchored Co atoms from Co/Zn-a$_g$ZIF-62-ipy exhibited higher electron density than that from Co/Zn-ZIF-62-ipy and Co(OAc)$_2$·4H$_2$O as the pre-edge negatively shifted to lower energy. Glassy Co/Zn-a$_g$ZIF-62-ipy demonstrates reduced white line peak intensity relative to Co/Zn-ZIF-62-ipy crystals, which can be attributed to diminished 1s→4p and increased 1s→3d electronic transitions, hence further corroborating the more tetrahedral geometry of Co in the glassy sample.[46,47]

The k^2-weighted Fourier transform spectra of extended X-ray absorption fine structure (EXAFS) for Co atoms from Co/Zn-ZIF-62-ipy and Co/Zn-a$_g$ZIF-62-ipy show a dominant peak at 1.5 Å (no phase-correction, Figure 3b). The peaks from Co/Zn-ZIF-62-ipy and Co/Zn-a$_g$ZIF-62-ipy at ca. 1.5 Å can be attributed to the Co—N/O bond and the Co—N bond, respectively. The absence of a discernible peak at ca. 2.4 Å (no phase-correction) confirms that there is no Co—Co scattering, therefore suggesting the atomic dispersion of Co in the crystal and glass ZIF materials.[48]

To obtain precise quantitative information for the Co coordination environment, EXAFS patterns of Co/Zn-ZIF-62-ipy and Co/Zn-a$_g$ZIF-62-ipy were fitted and are shown in Figure S14. The metrical fitting parameters are listed in Tables S3 and S4. At the starting model, the EXAFS fitting was performed with the first two shells in both samples. The value of σ for the higher-order shells was constrained to vary between ±0.04 relative to the previous shell, and other parameters were kept free to vary. In Co/Zn-ZIF-62-ipy, Co atoms are tetrahedrally coordinated with N/O atoms. The bond length for the Co—N bond was found to be about 2.046 Å and for the Co—O bond it was about 2.267 Å. For the second and third coordination shells, which are mainly filled with C, the bond lengths are 3.000 and 3.576 Å. In contrast, the fitting result shows the Co atoms from Co/Zn-a$_g$ZIF-62-ipy were surrounded by N in the first shell with a slightly shrunk bond length of ca. 2.006 Å, which is attributed to the collapse on the formation of a dense glassy structure. Moreover, it is note-
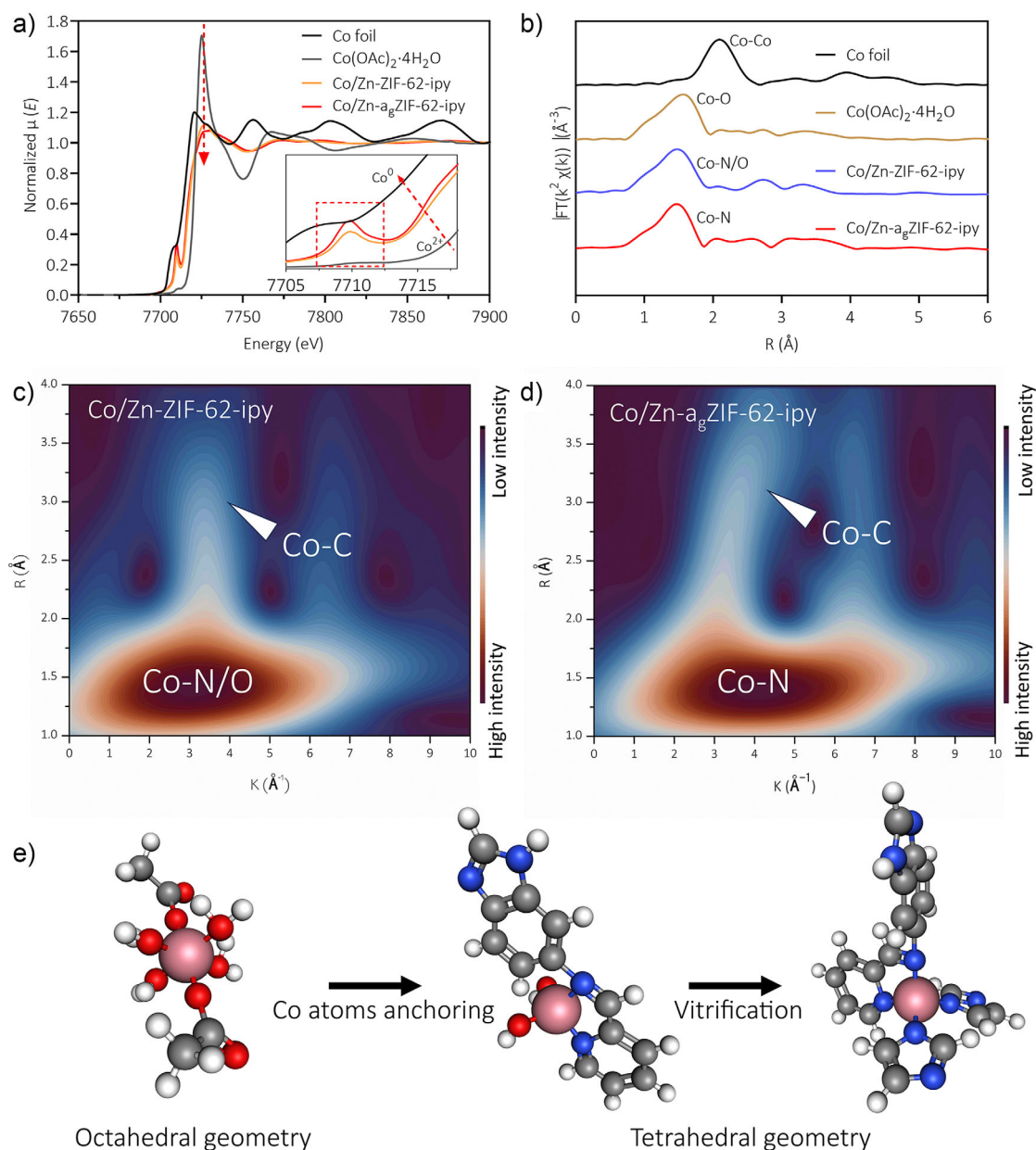
Figure 3. a) Co K-edge XANES spectra. The inset is an enlargement of the Co pre-edge peak. b) EXAFS for Co foil, $Co(OAc)_2 \cdot 4H_2O$, Co/Zn-ZIF-62-ipy, and Co/Zn-a_gZIF-62-ipy, respectively. c) WT plot for Co from Co/Zn-ZIF-62-ipy. d) WT plot for Co from Co/Zn-a_gZIF-62-ipy. e) Cobalt local coordination environment changed upon anchoring and vitrification. Co, O, C, H, and N atoms are represented as pink, red, grey, white, and blue spheres, respectively.

worthy to point out that the coordination number for the first Co—N shell is 3.76, which is slightly lower than that of an ideal tetrahedral geometry. The modest decrease from the typical 4 coordination number tetrahedral geometry can be attributed to the formation of ligand vacancies. These vacancies also illustrate the potential of electron-withdrawing ability upon light irradiation after the melt-quenching, when a rearrangement of the Co coordination environment occurs. The Co-C1 bond length remains unchanged in the second shell, whereas the Co-C2 bond shrank from 3.576 to 3.499 Å after vitrification, which means the C atoms are more closely packed due to the formation of shorter interatomic Co-C2 distance.

In addition, the wavelet-transfer (WT) plot visualizes the detailed Co coordination environment both before and after the vitrification process (Figure 3c,d). The carbon atoms formed the second and third shell of the anchored Co atoms in an ordered manner within the crystalline Co/Zn-ZIF-62-ipy, predominantly situated within the range of 2.5–3.0 Å (no phase-correction). In contrast, the carbon atoms surrounding Co atoms in Co/Zn-a_gZIF-62-ipy exhibit a significantly disordered configuration as the carbon atoms are distributed over a broader range of 2.5–4.0 Å (no phase-correction) with a heightened intensity as shown in Figure 3d. This further confirms that the C atoms around the Co
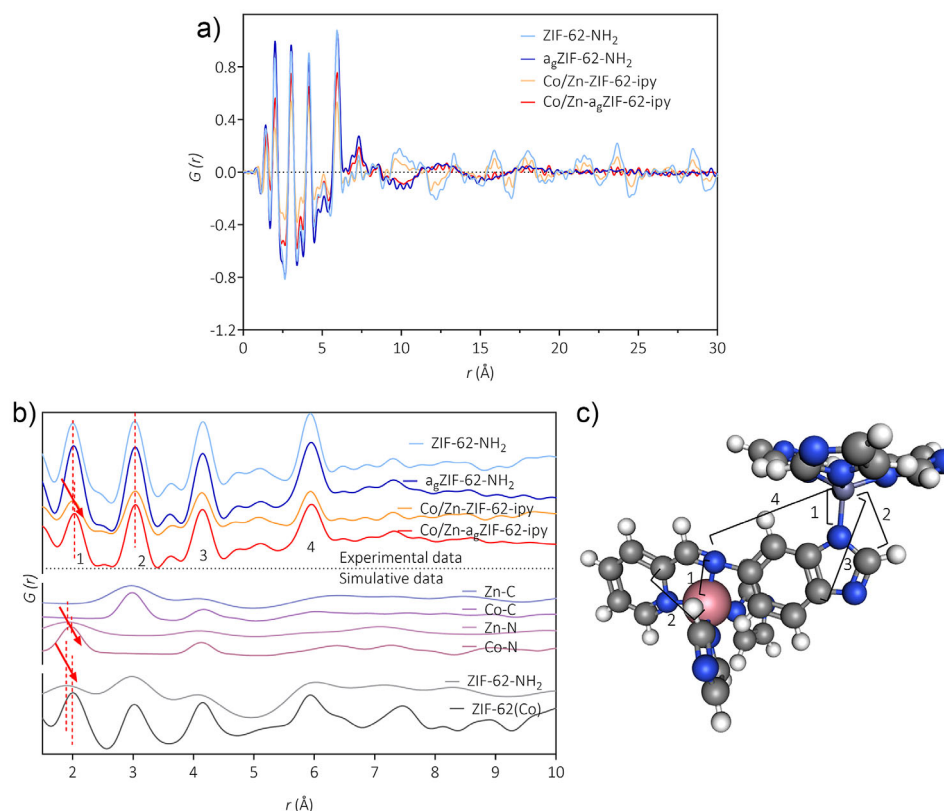
Figure 4. a) PDFs of ZIF-62-NH$_2$, a$_g$ZIF-62-NH$_2$, Co/Zn-ZIF-62-ipy, and Co/Zn-a$_g$ZIF-62-ipy between 0 and 30 Å, highlighting the absence of long-range order in glassy samples. b) PDFs between 1.5 and 10 Å, exhibiting similarities in short-range order. The red arrows show a slight shift in the atom pair distance, aligning with simulated observation that Co–N pairs resulted in a slightly longer average distance. c) Selected peak assignments are highlighted in the diagram of the hypothetic local Schiff base structure of Co/Zn-a$_g$ZIF-62-ipy. Zn, Co, C, H, and N atoms are represented as purple, pink, grey, white, and blue spheres, respectively.

atoms are less ordered and more closely packed in glassy materials.

Additionally, in situ synchrotron THz/Far-IR spectroscopy characterization was performed for Co/Zn-ZIF-62-ipy (Figure S15). Figure S15(A) shows the peak at ca. 305 cm^{-1} associated with the Zn-imidazolate stretching gradually shifts to ca. 290 cm^{-1} upon heating from room temperature to 300 °C. The primary cause of this phenomenon is ascribed to the distortion of the Zn-imidazolate bond and the oscillations occurring between the Co atoms and disturbed imidazolate ligands, leading to the gradual formation of Co-imidazolate bonds.[43–44] This occurs as the electron-withdrawing Co-imipyridine groups attract negatively charged imidazolate ligands and form a tetrahedral coordination environment around Co, resulting in Co atoms with increased electron density, as confirmed by XAS characterization (Figure 3e).[44] Furthermore, the second derivative of the in situ THz/Far-IR spectra showed the emergence of peak shifting in the temperature range 250–300 °C (Figure S15(B)), which aligns with the LLT behavior and Co XAS analysis.

Local Structure of Co/Zn-ZIF-62-ipy and Co/Zn-a$_g$ZIF-62-ipy

The synchrotron X-ray total scattering technique was utilized to investigate the local structures of crystalline Co/Zn-ZIF-62-ipy and the corresponding melt-quenched glass Co/Zn-a$_g$ZIF-62-ipy (raw data as shown in Figure S16). Pair distribution functions (PDFs) of crystalline and glassy materials were obtained from the Fourier transformation of the corrected total scattering data (Figure 4).

The crystalline ZIF-62-NH$_2$ and Co/Zn-ZIF-62-ipy exhibit long-range oscillations in the *G(r)* on scales ranging from 10–30 Å, as anticipated. In contrast, the PDF patterns of amorphous samples are essentially featureless in this region (Figure 4a). The amorphous phase of the glass is confirmed by the absence of identifiable correlations over 10 Å.[49]

The PDF profiles for crystal and glass are similar below 8 Å (Figure 4b). The peak at 2.00 Å of a$_g$ZIF-62-NH$_2$ is assigned to Zn–N pairs. In contrast, the peak labeled 1 in Figure 4b,c, which corresponds to the nearest Zn–N and Co–N distance of Co/Zn-a$_g$ZIF-62-ipy, was situated at 2.03 Å. This suggests that the introduction of a low quantity of Co–N pairs resulted in a slightly longer average distance between the metal and nitrogen than the distance of Zn–N pairs from a$_g$ZIF-62-NH$_2$. This is consistent with the trend of simulated patterns, which indicates that the distance of Co–N is longer than that of Zn–N (simulated Zn–N and Zn–C curves are based on the reported ZIF-62-NH$_2$ CIF file (CSD deposition 2115059), simulated Co–N and Co–C curves are based on the ZIF-62(Co) CIF file (CCDC deposition 1849807)). The peak at 3.1 Å (labeled 2 in Figure 4b,c) corresponds to the
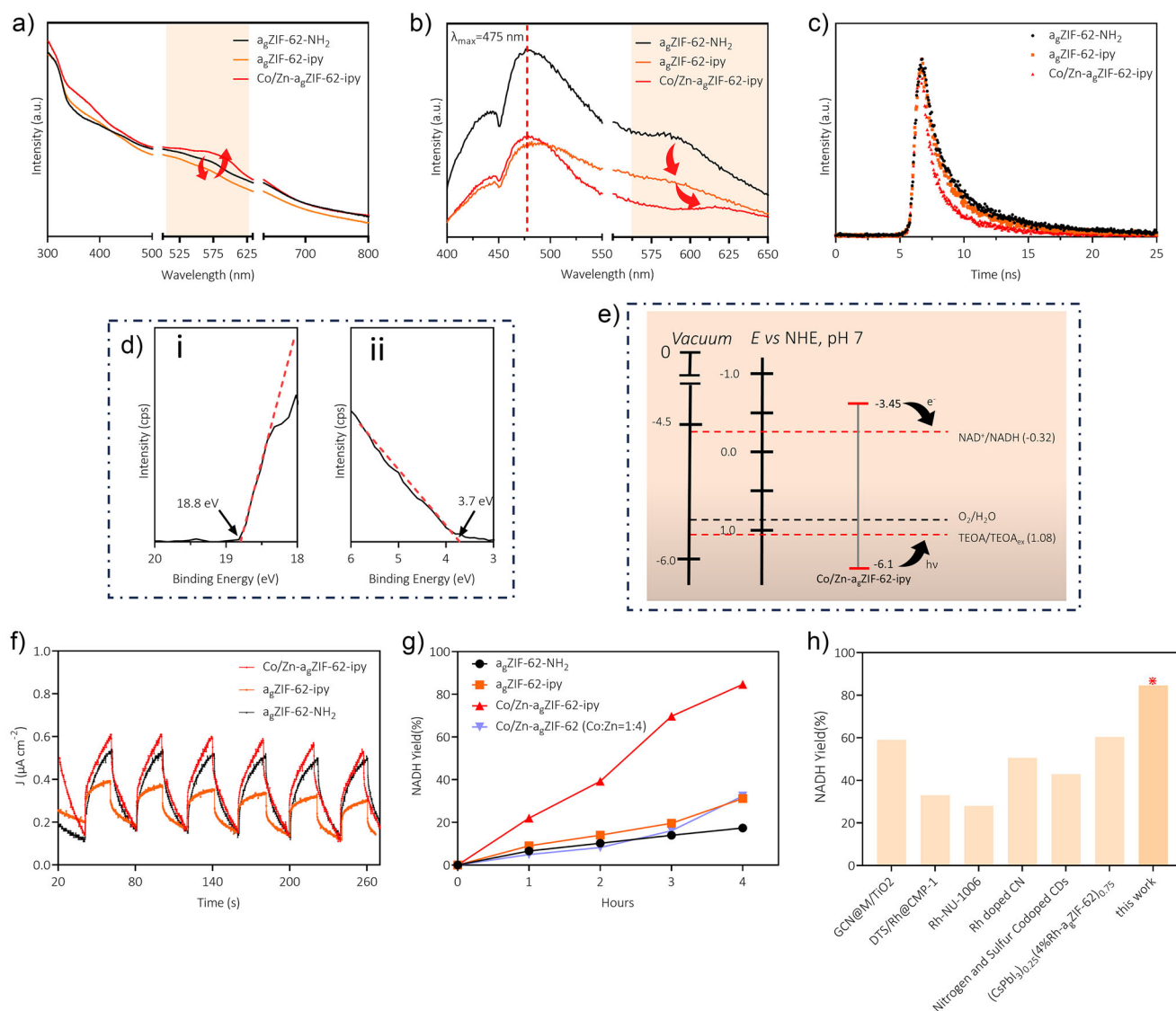
Figure 5. a) UV–vis DRS spectra of glassy samples; the red arrows denote the decrease and increase in light absorption. b) PL spectroscopy at ambient temperature; the red arrows indicate the change in PL due to modification. c) TRPL spectroscopy. d) UPS spectra of the (i) cut-off region and (ii) valence band edge region for Co/Zn-agZIF-62-ipy. e) Electronic band edges for Co/Zn-a_gZIF-62-ipy and photocatalytic reaction pathway. f) Transient photocurrent response obtained under visible light irradiation at a bias of 1.21 V. g) Time course of photocatalytic regeneration of NADH. h) Comparison of NADH yields between this work and the literature summarized in Table S5.

nearest Zn–C and Co–C. Correlations 3 and 4 are dominated by interactions between metal sites and light atoms from four neighboring ligands. These characteristics indicate that the crystal-glass phase transition of Co/Zn-ZIF-62-ipy did not alter the overall short-range order. The peak assignment was carried out based on the proposed hypothetic structure, as shown in Figure 4c.

Optical, Electrical Properties, and Photocatalysis Performance

The band edges (conduction band, CB, and valence band, VB) of MOF glasses can have a significant impact on their opto-electronic and photocatalytic performance. UV–vis diffuse reflectance spectroscopy (DRS), photoluminescence (PL),

and UV photoelectron spectrometry (UPS) were utilized to investigate the band positions in the original and modified glasses. The glassy samples a_gZIF-62-NH_2 and a_gZIF-62-ipy exhibited similar behaviors in light absorption, with the exception of a_gZIF-62-ipy displaying a decreasing absorption shoulder range from 500–600 nm due to the modification of the amino functional group (Figure 5a). In contrast, the Co/Zn-a_gZIF-62-ipy exhibited enhanced light absorption in this range as a result of the incorporation of Schiff base–Co moieties (Figure 5a). It is well known that a semiconductor such as TiO$_2$ can be modified by transition metal doping, resulting in an additional electron donor level contributed by doped ions and enhanced light adsorption at certain wavelengths.[50–52] The function of doped ions is similar to a photosensitizer. Such a scenario was observed from the

Co/Zn-a$_g$ZIF-62-ipy, where the enhanced light adsorption at ca. 600 nm is attributed to the local structure of tetrahedrally coordinated Co ions.[53] PL measurements further support these findings. The PL intensity at ca. 475 nm exhibited a significant decrease upon the functionalization process involving iminopyridine and subsequent metalation with Co (Figure 5b). This indicates possible prohibited electron-hole recombination and the enhanced transfer behavior of carriers. Moreover, the PL intensity at approximately 600 nm decreased following the functionalization of the amino group, which was consistent with the decrease in light absorption at approximately 500–600 nm. Conversely, the Co/Zn-a$_g$ZIF-62-ipy exhibits an increased PL at approximately 620 nm, consistent with its enhanced light absorption at around 600 nm. The electron-withdrawing effect can be further confirmed by the time-resolved photoluminescence (TRPL) spectra, as shown in Figure 5c. The carriers' lifetime of a$_g$ZIF-62-ipy was shorter than that of a$_g$ZIF-62-NH$_2$, and it was further reduced for the Co/Zn-a$_g$ZIF-62-ipy. This observation once again supports the electron-withdrawing properties of the Co atoms in Co/Zn-a$_g$ZIF-62-ipy as the shortest carrier lifetime indicates an efficient and rapid form of carrier transfer and electron capture via Co ion functionalized ligands.

The optical bandgap (E_g) of Co/Zn-a$_g$ZIF-62-ipy obtained from the Tauc plot (Figure S17) is ca. 2.65 eV. To determine the precise band positions, UV photoelectron spectroscopy (UPS) was conducted on Co/Zn-a$_g$ZIF-62-ipy and the VB was estimated to be ~-6.1 eV, whereas the CB was estimated to be ~-3.45 eV (vacuum level, Figures 5d and S18). Based on the above characterizations, Figure 5e shows the electronic band structure and the photocatalytic pathway of Co/Zn-a$_g$ZIF-62-ipy. The electronic band structure is also consistent with the bandgap energy calculated from steady-state PL spectra ($E_g = 1240/\lambda_{max}$, ca. 2.61 eV in this case, Figure 5b). Moreover, the photoelectrochemical properties were elucidated by photocurrent response. As shown in Figure 5f, a$_g$ZIF-62-NH$_2$ and a$_g$ZIF-62-ipy exhibited a photocurrent density of ~0.5 and ~0.38 μA cm^{-2}, respectively. This drop in photocurrent density is due to the partial modification of ligands. In contrast, the Co metalation sample Co/Zn-a$_g$ZIF-62-ipy exhibited the highest photocurrent density of ~0.60 μA cm^{-2}. This improved photocurrent response indicates that the Co center can extract a greater number of available charge carriers for photocatalytic applications than the unmodified material.

Based on the above findings, Co/Zn-a$_g$ZIF-62-ipy was proposed as a novel and effective glassy photocatalyst due to its unique structural and optical properties. To evaluate its catalytic performance, experiments were conducted on the photocatalytic regeneration of NADH, an essential coenzyme in biological redox reactions. As shown in Figure 5g, Co/Zn-a$_g$ZIF-62-ipy exhibited exceptional photocatalytic activity, achieving the highest NADH productivity of 211.5 μmol·g^{-1}·h^{-1}, which is nearly 5 times higher than that of the unmodified samples (a$_g$ZIF-62-NH$_2$, 43.4 μmol·g^{-1}· h^{-1}), despite both glassy materials showing similar gas sorption behavior and pore size distribution (Figure S19). To further distinguish the properties of anchored Co atoms and modified linkers from Co/Zn-a$_g$ZIF-62-ipy, the photocatalytic performance of Co/Zn-a$_g$ZIF-62-ipy was compared to the Co-based MOF glass a$_g$ZIF-62(Co) (detailed synthesis procedure available in Supporting Information) and a Co-doped bimetallic Zn-MOF glass with a Co/Zn ratio of 1:4 (Co/Zn-a$_g$ZIF-62, detailed synthesis procedure available in Supporting Information). The a$_g$ZIF-62(Co) was not stable during the photocatalytic test and all the solid-state a$_g$ZIF-62(Co) disintegrated after 1 h of light irradiation (as shown in Figure S20, the reaction system turned to purple due to the dissolution of a$_g$ZIF-62(Co)). In contrast, Co/Zn-a$_g$ZIF-62-ipy maintained its stability throughout the photocatalytic test, with a superior NADH regeneration performance in comparison to Co/Zn-a$_g$ZIF-62, making it one of the best performing catalysts compared with previously reported photocatalysts (Figure 5h and Table S5). Moreover, the catalyst Co/Zn-a$_g$ZIF-62-ipy after photocatalysis reaction was recycled for XPS analysis. The Co 2p XPS spectra (Figure S21) prior to and after photocatalysis reaction showed no significant changes, which further substantiated the stability of Co atoms within glassy matrix. This significant improvement in stability and photocatalytic performance again underscores the synergistic effect of the incorporated Co atoms and functionalized ligands within the glassy structure, which is expected to facilitate electron transfer and light absorption.

Furthermore, the luminance of the photocatalytic product was analyzed and the results unequivocally verified that the regenerated product was biologically active NADH (Figure S22). This finding underscores the potential of Co/Zn-a$_g$ZIF-62-ipy as a highly efficient photocatalyst for applications in biocatalytic processes and other light-driven biochemical transformations.

Conclusion

In summary, we demonstrated a new and effective approach to generating functionalized MOF glass through postsynthetic modification followed by thermal treatment. Vitrification of the Co-anchored meltable MOF (Co/Zn-ZIF-62-ipy) produced uniform and stable bimetallic framework glasses. The resultant bimetallic MOF glass exhibited enhanced photocurrent density compared to the Co-doped ZIF-62 glasses. Notably, the bimetallic glass achieved stable photocatalytic NADH regeneration, with an efficiency nearly five times that of the unmodified glass. This liquid modulation strategy offers an effective method for preparing MOF glass with evenly distributed dual-metal centers and Schiff base-metal complexes, enabling tailored optical properties for photocatalysis and the emulation of bimetallic enzyme functions.

Acknowledgements

Conflict of Interests

The authors declare no conflict of interest.

Data Availability Statement

The data that support the findings of this study are available in Supporting Information of this article.

Keywords: MOF glass · Liquid–liquid transition · Photocatalysis

[1] S. Zhang, S. Liu, Y. Sun, S. Li, J. Shi, Z. Jiang, *Chem. Soc. Rev.* **2021**, *50*, 13449–13466.

[2] Y. Sun, J. Shi, Z. Wang, H. Wang, S. Zhang, Y. Wu, H. Wang. Li, Z. Jiang, *J. Am. Chem. Soc.* **2022**, *144*, 4168–4177.

[3] Q. Xiang, Y. Huang, S. H. Jiang, S. X. Cheng, X. Li, T. Cai, *Adv. Funct. Mater.* **2024**, *34*, 2400512.

[4] F. Hollmann, A. Schmid, E. Steckhan, *Angew. Chem. Int. Ed.* **2001**, *40*, 169–171.

[5] Y. Zhang, Y. Zhao, R. Li, J. Liu, *Sol. RRL* **2021**, *5*, 2000339.

[6] S. Fukuzumi, Y.-M. Lee, W. Nam, *J. Inorg. Biochem.* **2019**, *199*, 110777.

[7] J. Liu, X. Ren, C. Li, M. Wang, H. Li, Q. Yang, *Appl. Catal. B: Environ.* **2022**, *310*, 121314.

[8] Y. Zhang, J. Liu, *Chem. Eur. J.* **2022**, *28*, e202201430.

[9] Y. Chen, P. Li, J. Zhou, C. T. Buru, L. Đorđević´, P. Li, X. Zhang, M. M. Cetin, J. F. Stoddart, S. I. Stupp, M. R. Wasielewski, *J. Am. Chem. Soc.* **2020**, *142*, 1768–1773.

[10] W. Liu, W. Hu, L. Yang, J. Liu, *Nano Energy* **2020**, *73*, 104750.

[11] C. Baffert, V. Artero, M. Fontecave, *Inorg. Chem.* **2007**, *46*, 1817–1824.

[12] P.-A. Jacques, V. Artero, J. Pécaut, M. Fontecave, *Proc. Natl. Acad. Sci. USA* **2009**, *106*, 20627–20632.

[13] J. A. Kim, S. Kim, J. Lee, J.-O. Baeg, J. Kim, *Inorg. Chem.* **2012**, *51*, 8057–8063.

[14] J. Lee, O. K. Farha, J. Roberts, K. A. Scheidt, S. T. Nguyen, J. T. Hupp, *Chem. Soc. Rev.* **2009**, *38*, 1450.

[15] H.-G. Jin, P.-C. Zhao, Y. Qian, J.-D. Xiao, Z.-S. Chao, H.-L. Jiang, *Chem. Soc. Rev.* **2024**, *53*, 9378–9418.

[16] K. Sun, Y. Huang, F. Sun, Q. Wang, Y. Zhou, J. Wang, Q. Zhang, X. Zheng, F. Fan, Y. Luo, J. Jiang, H.-L. Jiang, *Nat. Chem.* **2024**, *16*, 1638–1646.

[17] J. Jiang, F. Wei, G. Yu, Y. Sui, *J. Nanomater.* **2015**, *2015*, 192174.

[18] W. K. Fan, M. Tahir, *Energy Convers. Manage.* **2022**, *253*, 115180.

[19] A. Nishinaga, H. Tomita, *J. Mol. Catal.* **1980**, *7*, 179–199.

[20] G. Yuan, Y. Tian, J. Liu, H. Tu, J. Liao, J. Yang, Y. Yang, D. Wang, N. Liu, *Chem. Eng. J.* **2017**, *326*, 691–699.

[21] K. C. Gupta, A. K. Sutar, *Coord. Chem. Rev.* **2008**, *252*, 1420–1450.

[22] W. Xu, B. Tu, Q. Liu, Y. Shu, C.-C. Liang, C. S. Diercks, O. M. Yaghi, Y.-B. Zhang, H. Deng, Q. Li, *Nat. Rev. Mater.* **2020**, *5*, 764–779.

[23] C. J. Doonan, W. Morris, H. Furukawa, O. M. Yaghi, *J. Am. Chem. Soc.* **2009**, *131*, 9492–9493.

[24] L. Chen, H.-F. Wang, C. Li, Q. Xu, *Chem. Sci.* **2020**, *11*, 5369–5403.

[25] S. A. Ahmed, D. Bagchi, H. A. Katouah, M. N. Hasan, H. M. Altass, S. K. Pal, *Sci. Rep.* **2019**, *9*, 19372.

[26] R. Lin, M. Chai, Y. Zhou, V. Chen, T. D. Bennett, J. Hou, *Chem. Soc. Rev.* **2023**, *52*, 4149–4172.

[27] A. M. Bumstead, I. Pakamore´, K. D. Richards, M. F. Thorne, S. S. Boyadjieva, C. Castillo-Blas, L. N. McHugh, A. F. Sapnik, D. S. Keeble, D. A. Keen, R. C. Evans, R. S. Forgan, T. D. Bennett, *Chem. Mater.* **2022**, *34*, 2187–2196.

[28] R. Lin, X. Li, A. Krajnc, Z. Li, M. Li, W. Wang, L. Zhuang, S. Smart, Z. Zhu, D. Appadoo, J. R. Harmer, Z. Wang, A. G. Buzanich, S. Beyer, L. Wang, G. Mali, T. D. Bennett, V. Chen, J. Hou, *Angew. Chem. Int. Ed.* **2022**, *61*, e202112880.

[29] J. Fonseca, T. Gong, L. Jiao, H.-L. Jiang, *J. Mater. Chem. A* **2021**, *9*, 10562–10611.

[30] T. D. Bennett, J.-C. Tan, Y. Yue, E. Baxter, C. Ducati, N. J. Terrill, H. H. M. Yeung, Z. Zhou, W. Chen, S. Henke, A. K. Cheetham, G. N. Greaves, *Nat. Commun.* **2015**, *6*, 8079.

[31] J. Song, L. Frentzel-Beyme, R. Pallach, P. Kolodzeiski, A. Koutsianos, W.-L. Xue, R. Schmid, S. Henke, *J. Am. Chem. Soc.* **2023**, *145*, 9273–9284.

[32] G. Lin, Y. Zhang, Y. Hua, C. Zhang, C. Jia, D. Ju, C. Yu, P. Li, J. Liu, *Angew. Chem. Int. Ed.* **2022**, *61*, e202206283.

[33] J. Geary, D. J. Xiao, *Chem. Mater.* **2024**, *36*, 4916–4928.

[34] C. C. Lu, T. Weyhermüller, E. Bill, K. Wieghardt, *Inorg. Chem.* **2009**, *48*, 6055–6064.

[35] I. Gerz, S. A. V. Jannuzzi, K. T. Hylland, C. Negri, D. S. Wragg, S. Øien-Ødegaard, M. Tilset, U. Olsbye, S. DeBeer, M. Amedjkouh, *Eur. J. Inorg. Chem.* **2021**, *2021*, 4762–4775.

[36] S. Couck, J. F. Denayer, G. V. Baron, T. Rémy, J. Gascon, F. Kapteijn, *J. Am. Chem. Soc.* **2009**, *131*, 6326–6327.

[37] H. R. Abid, J. Shang, H.-M. Ang, S. Wang, *Int. J. Smart Nano Mater.* **2013**, *4*, 72–82.

[38] Y. Zhang, C. Xie, Y. Zhi, Q. Sun, X. Luo, Z. Li, J. Wang, X. Liu, *Polymer* **2021**, *212*, 123307.

[39] N. Popp, T. Homburg, N. Stock, J. Senker, *J. Mater. Chem. A* **2015**, *3*, 18492–18504.

[40] O. A. Ali, S. M. El-Medani, D. A. Ahmed, D. A. Nassar, *J. Mol. Struct.* **2014**, *1074*, 713–722.

[41] A. R. Stefankiewicz, M. Wałęsa-Chorab, H. B. Szcześniak, V. Patroniak, M. Kubicki, Z. Hnatejko, J. Harrowfield, *Polyhedron* **2010**, *29*, 178–187.

[42] J. Choi, A. Thirupathi, J. Kim, H.-J. Ha, K.-H. Ahn, E. J. Kang, *J. Org. Chem.* **2024**, *89*, 18081–18089.

[43] M. R. Ryder, B. Civalleri, T. D. Bennett, S. Henke, S. Rudić, G. Cinque, F. Fernandez-Alonso, J.-C. Tan, *Phys. Rev. Lett.* **2014**, *113*, 215502.

[44] J. Hou, M. L. Ríos Gómez, A. Krajnc, A. McCaul, S. Li, A. M. Bumstead, A. F. Sapnik, Z. Deng, R. Lin, P. A. Chater, D. S. Keeble, D. A. Keen, D. Appadoo, B. Chan, V. Chen, G. Mali, T. D. Bennett, *J. Am. Chem. Soc.* **2020**, *142*, 3880–3890.

[45] S. Frank, M. Folkjær, M. L. Nielsen, M. J. Marks, H. S. Jeppesen, M. Ceccato, S. J. Billinge, J. Catalano, N. Lock, *J. Mater. Chem. A* **2024**, *12*, 781–794.

[46] W. Huang, B. Chan, Y. Yang, P. Chen, J. Wang, L. Casey, C. Atzori, T. Schulli, O. Mathon, H. G. Hackbarth, N. M. Bedford, D. Appadoo, X. Li, T. Lin, R. Lin, J. Lee, Z. Wang, V. Chen, A. K. Cheetham, L. Wang, J. Hou, *J. Am. Chem. Soc.* **2025**, *147*, 3195–3205.

[47] F. Carraro, O. Vozniuk, L. Calvillo, L. Nodari, C. La Fontaine, F. Cavani, S. Agnoli, *J. Mater. Chem. A* **2017**, *5*, 20808–20817.

[48] M. Gupta, Y. Kumar, A. Tayal, N. Pandey, W. Caliebe, J. Stahn, *SN Appl. Sci.* **2020**, *2*, 41.

[49] C. Ye, G. I. Lampronti, L. N. McHugh, C. Castillo-Blas, A. Kono, C. Chen, G. P. Robertson, L. A. V. Nagle-Cocco, W. Xu, S. D. Stranks, V. Martinez, I. Brekalo, B. Karadeniz, K. Užarević, W. Xue, P. Kolodzeiski, C. Das, P. Chater, D. A. Keen, S. E. Dutton, T. D. Bennett, *Chem. Sci.* **2024**, *15*, 7198–7205.

[50] R. Niishiro, R. Konta, H. Kato, W.-J. Chun, K. Asakura, A. Kudo, *J. Phys. Chem. C* **2007**, *111*, 17420–17426.

[51] Z.-M. Dai, G. Burgeth, F. Parrino, H. Kisch, *J. Organomet. Chem.* **2009**, *694*, 1049–1054.

[52] B. Choudhury, A. Choudhury, *J. Lumin.* **2012**, *132*, 178–184.

[53] S. A. Mansour, A. H. Farha, M. F. Kotkata, *J. Inorg. Organomet. Polym. Mater.* **2019**, *29*, 1375–1382.